IOP Publishing Journal of Physics D: Applied Physics

J. Phys. D: Appl. Phys. **50** (2017) 265303 (9pp) https://doi.org/10.1088/1361-6463/aa7489

On the phase transformation of single-crystal 4H–SiC during nanoindentation

Mitsuhiro Matsumoto[1], Hu Huang[1], Hirofumi Harada[2], Koichi Kakimoto[2] and Jiwang Yan[1]

[1] Department of Mechanical Engineering, Keio University, Hiyoshi 3-14-1, Kohoku-ku, Yokohama 223-8522, Japan
[2] Research Institute for Applied Mechanics, Kyushu University, 6-1 Kasuga-Koen, Kasuga 816-8580, Japan

E-mail: yan@mech.keio.ac.jp

Received 22 March 2017, revised 18 May 2017
Accepted for publication 22 May 2017
Published 12 June 2017

Abstract

Microstructural changes of single-crystal 4H silicon carbide (SiC) induced by nanoindentation under various conditions were investigated. It was found that nanoindentation at different crystal orientations induced different Raman spectroscopic characteristics. Cross-sectional observation by transmission electron microscopy indicated that a very deep subsurface damage region was formed where dislocations occurring along the basal planes, crystal grains rotation and micro-cracks were observed. The microstructures of the damage regions were strongly affected by the nanoindentation conditions. Coupled analysis of lattice fringes and Raman spectra indicated that a phase transformation from 4H–SiC to 3C–SiC occurred during nanoindentation, which has never been reported before. Furthermore, the 4H to 3C phase transformation strongly depended on the indenter orientation with respect to the SiC crystal. These findings are meaningful for low-damage precision machining of SiC substrates.

Keywords: nanoindentation, single-crystal silicon carbide, crystal orientation, phase transformation, subsurface damage, dislocation

(Some figures may appear in colour only in the online journal)

1. Introduction

Taking features of excellent bandgap, breakdown field, thermal conductivity and stability [1, 2], single-crystal silicon carbide (SiC) is regarded as the most promising next-generation 'post silicon' semiconductor material that works under high temperature and/or high voltage. The manufacturing of high-quality SiC wafers is an essential technical step for future power electronic device industry. However, the precision machining of defect-free SiC substrates is still technically difficult due to the high hardness and brittleness as well as the strong anisotropy of the material. In diamond turning and slicing of SiC, severe tool wear occurs, and a very deep subsurface damage layer is generated into the workpiece [3–5]. Subsurface damage also occurs in electrical discharge machining of SiC [6, 7]. Although the subsurface damage layer may be gradually removed by subsequent grinding [8] and chemo/mechanical polishing [9, 10] processes, the material removal rate is extremely low, leading to an unacceptably long time to obtain a mirror finish. To reduce the polishing time, one of the essential tasks is to reduce the depth of subsurface damage.

The existing mechanical machining technologies for SiC are mostly based on or renovated from those developed for single-crystal silicon, although there are distinct differences in material properties between these two kinds of materials. The lack of unique machining technologies for SiC is mainly because there is very limited literature on the microscopic mechanical properties and nanometer scale machining/deformation mechanisms for SiC.

Nanoindentation has been confirmed to be a powerful method for investigating mechanical behaviors and microstructural changes of materials in the nanometer scale [11]. This is because the situation of mechanical contact between an indenter and a specimen in nanoindentation is geometrically akin to that between an abrasive grain and a workpiece

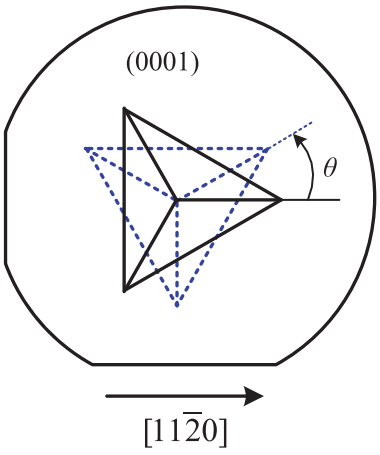

Figure 1. Schematic diagram for the definition of indenter orientation angle θ.

in slicing, grinding, and lapping. That is to say, an indenter can be used to simulate a cutting tool tip or an abrasive grain in mechanical machining. Hence, clarifying the indentation-induced material responses including deformation, fracture and microstructural change of a material can provide important information for clarifying the machining mechanisms, improving surface integrity, and developing new manufacturing technologies for that material.

In the past several decades, there have been a great number of studies on nanoindentation of silicon wafers [12–18] which have significantly contributed to the advance of manufacturing technologies of high quality silicon wafers. On the other hand, literature on nanoindentation of single-crystal SiC is still very little, although a few authors carried out molecular dynamics simulation on it [19]. The subsurface damage of 6H–SiC in nanoindentation tests was experimentally investigated by Yan *et al* [20], and a very deep subsurface damage region was confirmed beneath the indenter where a phase transformation from single crystal to nano poly-crystal occurred. Goel *et al* [21] studied the incipient plasticity of 4H–SiC by nanoindentation at very low indentation depths and reported that elastic-to-plastic transition occurred when the shear stress was over 21 GPa. Matsumoto *et al* [22] investigated the hardness dependence of 4H–SiC by nanoindentation, and found that when the indenter ridge was parallel to the [1 1 $\bar{2}$ 0] direction, 4H–SiC showed the lowest hardness. More recently, Nawaz *et al* [23] used nanoindentation to investigate the nanometer scale elastic-plastic properties of 4H–SiC, and further observed the deformation behaviors beneath the indent via transmission electron microscopy (TEM). However, up to date, the phenomena and mechanisms of mechanical contact-induced phase transformations of 4H–SiC have not been clarified.

In this paper, by performing nanoindentation tests under various loading conditions and crystal orientations and subsequent microstructure analysis via Raman spectroscopy and transmission electron microscopy, phase transformation characteristics of 4H–SiC were comparatively studied. It is expected that the results in this study can enhance the understanding of mechanical contact-induced phase transformation in 4H–SiC and provide useful information for the development and optimization of the nanometer scale precision machining processes for high-quality SiC substrates.

2. Materials and experiments

3C–SiC, 4H–SiC, and 6H–SiC are the most common structures in SiC polymorphs. Compared to 3C–SiC and 6H–SiC, 4H–SiC has wider bandgap and higher electron mobility. Furthermore, 4H–SiC shows a much higher ductile to brittle transition depth, suggesting better machinability and cost effective production [21]. Accordingly, 4H–SiC has attracted more attention from both scientific and industrial communities. Thus, 4H–SiC was selected as the research object in this study. An *n*-type single-crystal 4H–SiC wafer, which has a (0 0 0 1) surface plane with a silicon face and an orientation flat along [1 1 $\bar{2}$ 0], was used for experiments. The wafer was 50 mm in diameter and 0.36 mm in thickness, and it had been chemomechanically polished to achieve a mirror surface with the surface roughness R_a less than 0.5 nm.

Nanoindentation tests were conducted at ambient temperature by using a commercially available ENT-1100a nanoindentation system (Elionix Inc., Japan). A standard Berkovich indenter made of single-crystal diamond was used in all the experiments. To study the effect of crystal orientation on indentation response, the indenter orientation angle θ was defined as the angle between the indenter ridge and the wafer orientation flat ([1 1 $\bar{2}$ 0] direction), as shown in figure 1. Previous studies [22, 24, 25] indicated that the indentation hardness of 4H–SiC showed strong anisotropy. When the indenter ridge was parallel to the $\langle 1\,1\,\bar{2}\,0\rangle$ direction, i.e. $\theta = 0°$, the indentation hardness was the lowest. When the indenter ridge was parallel to the $\langle 1\,\bar{1}\,0\,0\rangle$ direction, i.e. $\theta = 30°$, the indentation hardness was the highest. Additionally, both the Berkovich indenter and the crystal structure of 4H–SiC are geometrically symmetrical, and thus, two representative indenter orientation angles, $\theta = 0°$ and 30°, were selected for comparison in this study. Furthermore, it was reported that the indentation hardness of 4H–SiC was also affected by the peak load and loading rate [22]. Thus, various peak loads (5, 40, and 100 mN) were selected for comparison. To ensure a same thermal drift during nanoindentation, the loading time (10 s), holding time at the peak load (1 s), and the unloading time (10 s) were kept consistent for most nanoindentation tests. As a result, various loading rates, 0.5, 4, and 10 mN s^{-1} were induced corresponding to the peak loads of 5, 40, and 100 mN, respectively. On the other hand, previous research [13, 17] indicated that the phase transformation of single-crystal silicon was very sensitive to the loading rate, and a relatively low loading rate readily induced the occurrence of phase transformation in silicon. Accordingly, a very low loading rate of 0.05 mN s^{-1} was selected as an exception for some nanoindentation tests with the peak load of 5 mN.

After nanoindentation, a laser micro-Raman spectrometer, NRS-3000 (JASCO, Tokyo, Japan), was used to detect the residual phases in the indents. The residual indent morphologies were observed by using a field emission scanning electron

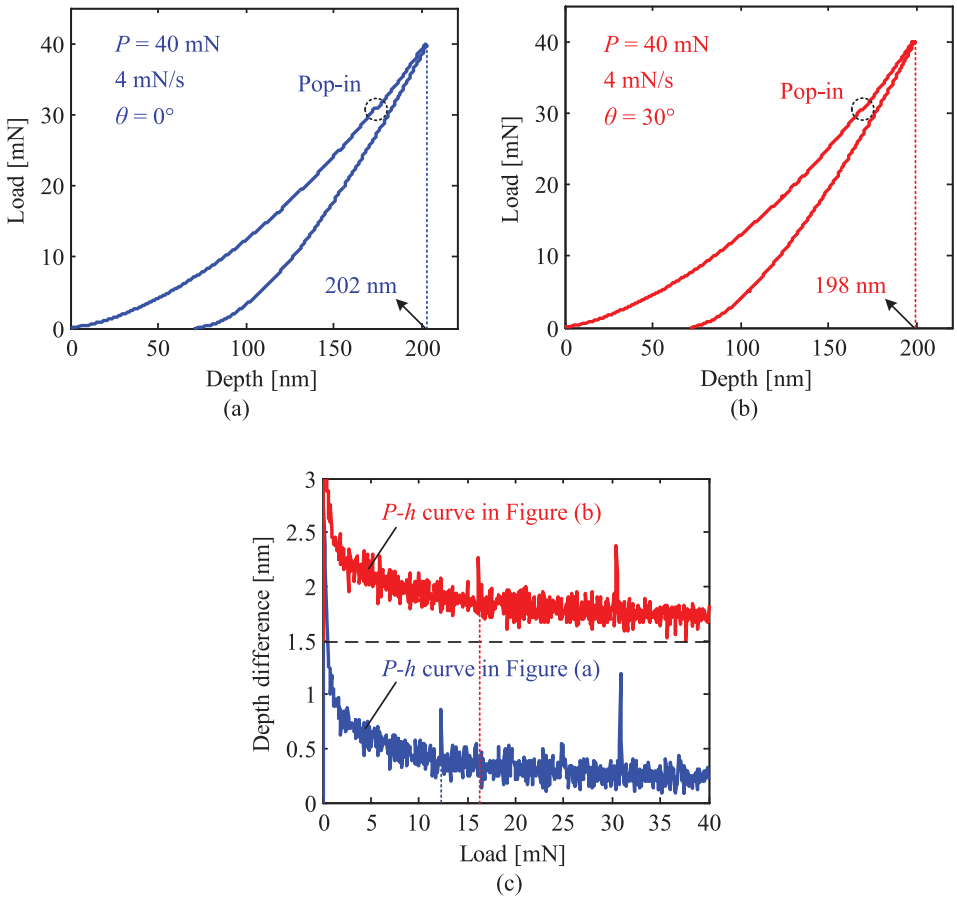

Figure 2. Typical load-depth (*P-h*) curves: (a) $P = 40$ mN, 4 mN s^{-1}, $\theta = 0°$, (b) $P = 40$ mN, 4 mN s^{-1}, $\theta = 30°$. (c) Depth difference curves for figures 2(a) and (b).

microscopy (FE-SEM), JSM-7600F (JEOL, Japan). The subsurface microstructures of the residual indents were observed by a transmission electron microscopy (TEM), Tecnai G2 (FEI Company, USA). The TEM samples were prepared by using a focused-ion beam (FIB) system, Quanta 3D FEG (FEI Company, USA).

3. Results and discussion

3.1. Load-depth (P-h) characteristics

Figure 2 shows representative load-depth (*P-h*) curves. Detailed experimental conditions are given in each figure. In figures 2(a) and (b), for a same peak load of 40 mN and loading rate of 4 mN s^{-1}, the maximum indentation depth is 202 nm for the indenter orientation angle $\theta = 0°$, while it is 198 nm for $\theta = 30°$. The difference in the maximum indentation depth implies that the hardness for $\theta = 0°$ is lower than that for $\theta = 30°$, which is further confirmed by their hardness values calculated by using the Oliver–Pharr method [26], 37.86 GPa for $\theta = 0°$ while 39.68 GPa for $\theta = 30°$. This agrees well with our previous results that the indentation hardness was the lowest when the indenter ridge was parallel to the $[1\,1\,\bar{2}\,0]$ direction [22].

Furthermore, remarkable pop-ins appear in the loading curves at a load of ~30 mN in figures 2(a) and (b). To clearly illustrate the pop-ins, the depth difference method, as used in [27], is used to amplify the locally discontinuous depth change in the *P-h* curves, and the comparative curves are presented in figure 2(c). A sharp peak in the depth difference curve corresponds to a pop-in and the height of the peak denotes the depth of the pop-in, i.e. the higher the peak, the deeper the pop-in. Corresponding to the pop-ins observed in figures 2(a) and (b), sharp peaks appear in the depth difference curves at ~30 mN. The peak height corresponding to figure 2(a) is slightly larger than that to figure 2(b), implying that the pop-in in figure 2(a) is deeper. Apart from the major pop-ins at ~30 mN, it is interesting to observe a few secondary pop-ins in figure 2(c). For $\theta = 0°$, the secondary pop-in appears at ~12 mN, while at ~16 mN for $\theta = 30°$. Furthermore, the secondary pop-in for $\theta = 0°$ is also deeper than that for $\theta = 30°$. Previous studies [17, 28, 29] on nanoindentation of single-crystal silicon indicated that a pop-in in the *P-h* curve might result from phase transformation, burst of dislocations, and cracks. When the indentation load is low, phase transformation and burst of dislocations play the dominant role, while at a high load, cracks become the main reason for pop-ins. Accordingly, the secondary pop-ins in figure 2(c) may result from phase transformation or burst of dislocations, while the major pop-ins may result from cracks due to the brittle nature of SiC. By further observing the residual indent morphologies via FE-SEM, we found that the critical indentation load for

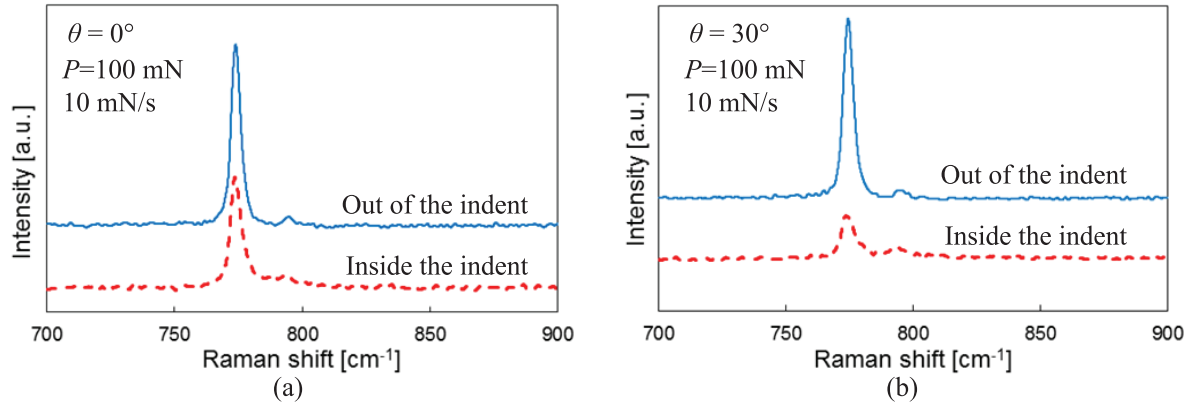

Figure 3. Comparison of Raman spectra obtained inside and out of the indents generated under a peak load of 100 mN: (a) $\theta = 0°$ and (b) $\theta = 30°$.

radial cracks is 30–34 mN, which agrees with the load for the occurrence of major pop-ins (~30 mN).

3.2. Raman spectroscopy

Residual phases in the indents were investigated by a laser micro-Raman spectrometer, which is commonly used to analyze crystal structure and residual stress of semiconductors. As the laser spot size for the Raman spectrometer is ~1 μm, a peak load of 100 mN with the loading rate of 10 mN s^{-1} was selected to generate indents with enough size for Raman testing. Figures 3(a) and (b) show the comparison of Raman spectra of SiC obtained inside and out of (100 μm far from) the indent, corresponding to $\theta = 0°$ and 30°, respectively. In figure 3(a), both the spectra show the typical crystal peaks of 4H–SiC [30, 31]. Although the difference in the peak intensity is observed, no new peaks are detected. In figure 3(b), the peak near 795 cm^{-1} has no change in intensity while the peak near 776 cm^{-1} is weaken inside the indent. Nakashima *et al* [31] reported that 4H–SiC has two peaks on FTO mode, 776 cm^{-1} and 796 cm^{-1}, and the peak near 776 cm^{-1} is stronger than that near 796 cm^{-1}. 3C–SiC has only one peak near 776 cm^{-1}. Therefore, the result in figure 3(b) indicates that the peak of 4H–SiC becomes weaker and that of 3C–SiC becomes stronger inside the indent.

For clarifying the ratio of the peak heights, the Raman spectra were decomposed into two Gaussian distributions, and approximation was applied to each of them. Figure 4 shows an example of the approximation result for the case $\theta = 0°$, and table 1 summarizes the peak heights inside and out of the indents and their ratios under different crystal orientations. The ratio was calculated by dividing the peak height near 796 cm^{-1} by the peak height near 776 cm^{-1}. The ratio obtained outside the indents for both $\theta = 0°$ and 30° is nearly the same, while that obtained inside the indents for $\theta = 30°$ is evidently larger than that for $\theta = 0°$. This result implies that the phase transformation might have occurred from 4H- to 3C–SiC for $\theta = 30°$.

It is well known that the full width at half maximum (FWHM) of the peak represents the degree of crystallinity. Table 2 shows the FWHMs of the Raman peaks near 776 cm^{-1}

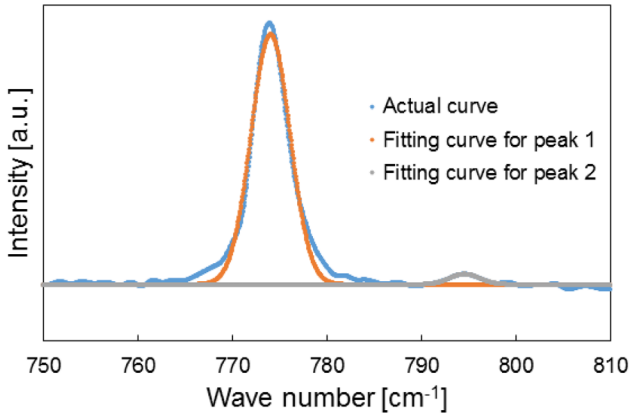

Figure 4. Example of approximation fitting of Raman peaks according to the Gaussian distribution.

obtained from four spectra in figure 3. For both θ, the FWHM obtained inside the indent is larger than that obtained out of the indent, demonstrating that the crystal structure had been disordered during indentation.

3.3. Cross-sectional TEM observation

To investigate the change of subsurface microstructure induced by nanoindentation, TEM samples were extracted from the residual indents generated under various peak loads, loading rates and indenter orientation angles θ. Table 3 summarizes the nanoindentation conditions for these samples.

Figure 5 shows a bright field TEM micrograph of sample A. In figure 5(a), the white triangle denotes the indenter tip. Obviously, the damaged depth below the indent is larger than the indentation depth. Figures 5(b)–(d) show the enlarged views corresponding to the regions b, c and d in figure 5(a), respectively. In figure 5(b), dislocations are observed on the basal plane which is parallel to the sample surface (0 0 0 1). Similar dislocations were previously reported for 4H- and 6H–SiC [20, 23]. These dislocation lines also appear for all the other TEM samples because of the slip systems in crystal SiC, i.e. $(0\,0\,0\,1)\langle 1\,\bar{2}\,1\,0\rangle$ or $(0\,0\,0\,1)\langle 0\,1\,\bar{1}\,0\rangle$ [20, 23]. In figure 5(c), micro-cracks in parallel direction appear although no crack is observed on the wafer surface. This indicates

Table 1. Summary of the peak height inside/outside the indents and their ratios under different crystal orientations.

		Peak (cm^{-1})		
		776	796	Ratio
$\theta = 0°$	Outside	44.75	1.869	4.18%
	Inside	25.71	2.237	8.70%
$\theta = 30°$	Outside	50.41	2.156	4.28%
	Inside	11.44	2.157	18.85%

Table 2. FWHMs of Raman peaks near 776 cm^{-1}.

	Outside	Inside	Ratio
$\theta = 0°$	4.37	5.14	118%
$\theta = 30°$	4.80	6.37	133%

Table 3. Nanoindentation conditions for TEM samples.

	Peak load (mN)	Loading rate (mN s^{-1})	θ (°)
Sample A	5	0.5	0
Sample B	5	0.05	0
Sample C	5	0.5	30
Sample D	100	10	0
Sample E	100	10	30

that the indentation load of 5 mN is over the critical load for crack occurrence, and subsurface cracks initiate at a smaller load than surface cracks. Accordingly, the secondary pop-ins in figure 2(c) might result from the burst of dislocations and micro-cracks beneath the indents. However, the individual role of dislocations and micro-cracks could not be identified in this study, and further investigation is required.

In figure 5(d), lattice fringes parallel to the sample surface (0 0 0 1) are observed. 31 fringes show a width of 7.81 nm and the average width for each fringe is calculated to be 0.252 nm, agreeing well with the interlayer spacing of 4H–SiC along c axis, 0.2513 nm. Furthermore, by fast Fourier transform (FFT), the interlayer spacing is also confirmed to be 0.258 nm. Thus, the lattice fringe in figure 5(d) denotes the basal plane of SiC.

Figure 6(a) presents the TEM micrograph of sample B and figure 6(b) shows the enlarged view of the region b in figure 6(a). Compared with the micrograph in figure 5(a), the micrograph in figure 6(a) exhibits a much larger damaged area, indicating that the lower loading rate induces larger indentation depth. This confirms that the decreased loading rate (0.05 mN s^{-1}) is beneficial for initiation and propagation of dislocations because they are thermally activated deformation processes. In figure 6(b), several stripes approximately perpendicular to the (0 0 0 1) face are observed and they could be a kind of rotation Moire pattern, which results from superposition of two lattices (with the same spacing d) at a rotation angle φ. The spacing of the enlarged lattice D can be expressed as

$$D = d/\varphi \tag{1}$$

By counting the number of the fringe, we obtained $D = 4.464$ nm, $d = 0.244$ nm, and $\varphi = 3.3°$, respectively. The value of φ is smaller than the angle between the sample surface (0 0 0 1) and the indenter edge (12.9°), which might be due to material elastic recovery during unloading.

Figure 7 shows the TEM micrograph of sample C. Similar to samples A and B, dislocations on the basal plane and micro-cracks are observed. In figure 7(b), the width of periodic fringes is obviously different from that of samples A and B. 24 fringes correspond to a total width of 24.36 nm, and thus the average width is calculated to be 1.015 nm, which is very close to the lattice constant of 4H–SiC along c axis, i.e. 1.0053 nm. Thus, each fringe in figure 7(b) includes four layers of the basal plane. The slight difference between the measured width and the lattice constant (the former is 1% larger than the latter) might result from the residual tensile stress inside the deformed region. Furthermore, in figure 7(c), lattice fringes with a specific angle of ~70° to (0 0 0 1) face appear which is featured in figure 7(d). This kind of lattice fringe is observed in the entire region enclosed by broken line in figure 7(a). 32 fringes is counted in 8.42 nm, and thus, the average width is 0.263 nm, which is a little larger than the interlayer spacing of 4H–SiC along c axis (0.2513 nm). The FFT pattern in figure 7(c) further confirms the existence of lattice fringes with the angle of ~70° to (0 0 0 1) face.

Figures 8(a) and (b) show the TEM micrographs of samples D and E, respectively. In addition to the dislocations observed on the basal plane for samples A–C, remarkable median cracks appear in samples D and E. The length of the median cracks is 2.7 μm for sample D, which is larger than that for sample E (2.4 μm). Furthermore, a small lateral crack is visible for sample D as shown in figure 8(a), while it is not observed for sample E in figure 8(b). The difference in subsurface cracks in samples D and E further confirms the orientation dependence of crack generation in 4H–SiC. The crack resistance for $\theta = 0°$ is smaller than that for $\theta = 30°$, agreeing well with the orientation dependence of the pop-in and hardness in figure 2. It should be noted that similar tilted lattice fringes with an angle of ~70° to (0 0 0 1) face are observed for sample E around the regions near the crack and just beneath the indent but they do not appear in sample D.

Although a previous study by molecular dynamics simulation reported that nanoindentation induced amorphization of SiC [32], no amorphous structure was observed in all the TEM samples in this study even by checking all the indentation affected regions in detail. This agrees with previous TEM observations of the deformation regions of SiC induced by nanoindentation [20, 23] where no amorphization was observed. On the other hand, a new kind of tilted lattice fringes with an angle of ~70° to (0 0 0 1) face is observed here in samples C and E indented with an indenter orientation angle $\theta = 30°$, suggesting a possible phase transformation from 4H–SiC to another SiC crystal structure. Combining the Raman spectra results in section 3.2, it is presumable that some 4H–SiC beneath the indenter has transformed into 3C–SiC for the case of $\theta = 30°$. However, for the case of $\theta = 0°$, this kind of phase transformation is not observed. This fact indicates that the phase transformation in 4H–SiC during nanoindentation is crystal orientation dependent, which has never been reported before.

Up to date, the phase transformation from 4H- to 3C–SiC has been rarely reported. During thermal oxidation of

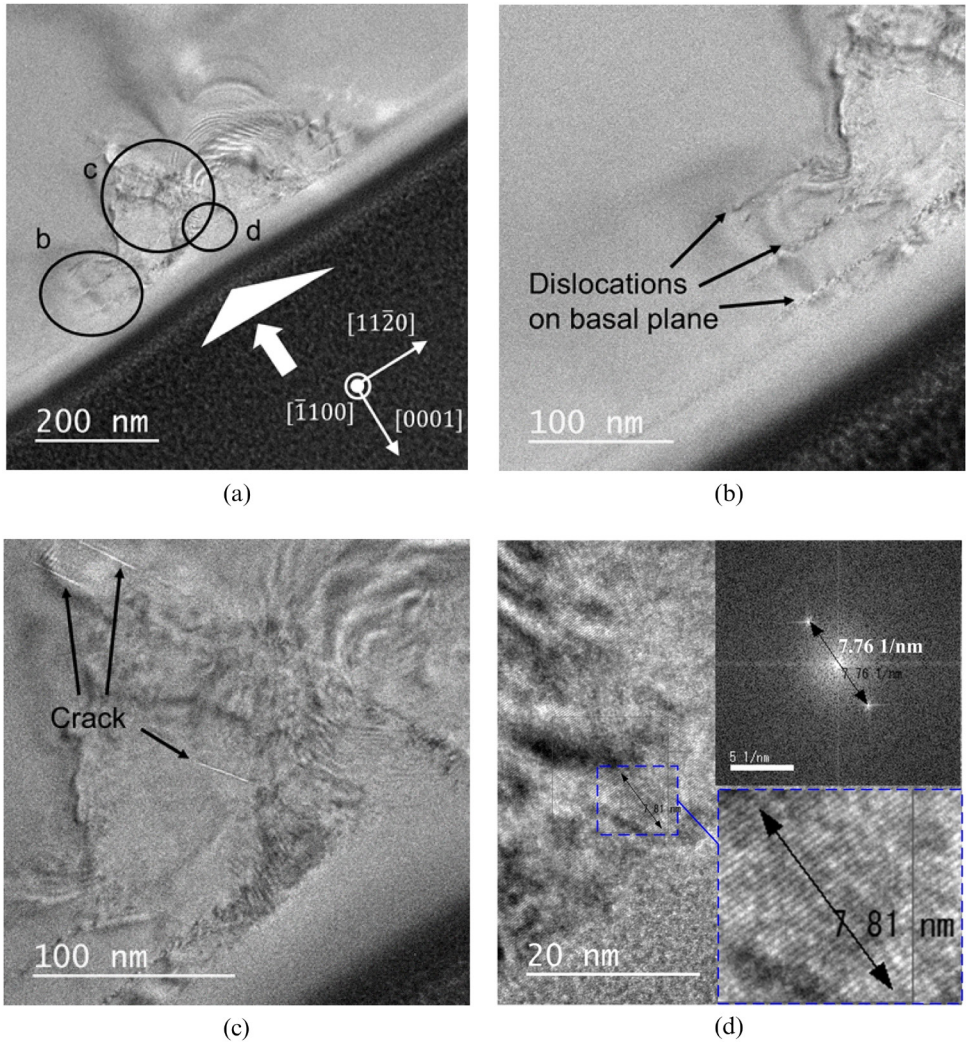

Figure 5. TEM micrographs of sample A: (a) general view, (b) basal slips, (c) micro-cracks, and (d) lattice fringe and its corresponding FFT pattern.

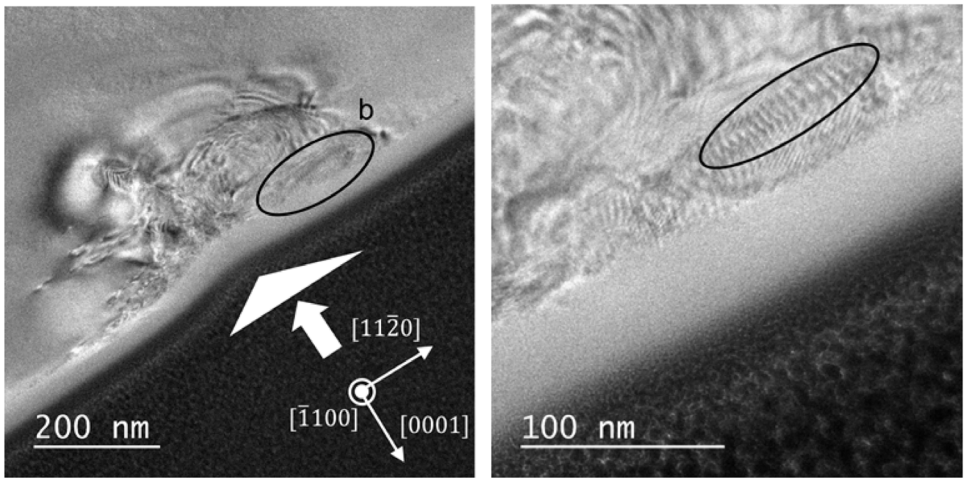

Figure 6. TEM micrographs of sample B: (a) general view, (b) Moire patterns.

4H–SiC, Okojie *et al* [33] reported the 4H to 3C polytypic transformation, which was tentatively attributed to the motion of 1/3$\langle 1\,0\,\bar{1}\,0\rangle$Shockley partial dislocations on basal (0 0 0 1) planes. Chen *et al* [34] reported the phase transformation from 4H- to 3C–SiC during *in situ* TEM compression of 4H–SiC nanopillar and they gave a more detailed phase transformation paths by the slip of 1/3$\langle 1\,\bar{1}\,0\,0\rangle$ direction on the (0 0 0 1) plane as shown in figure 9(a), where A, B and C denote three

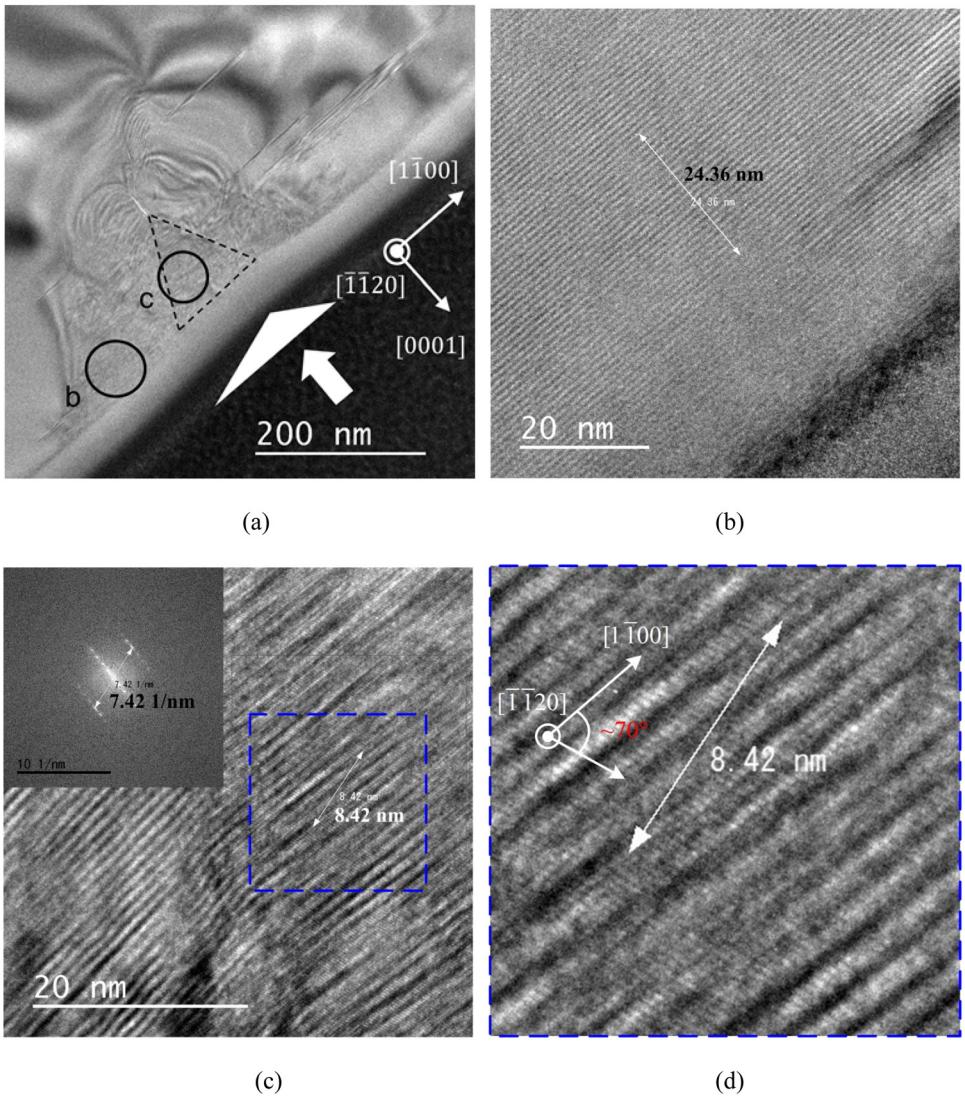

(a) (b)

(c) (d)

Figure 7. TEM micrographs of sample C: (a) general view, (b) periodical fringes, (c) lattice fringe and its corresponding FFT pattern, and (d) enlarged view of figure 7(c).

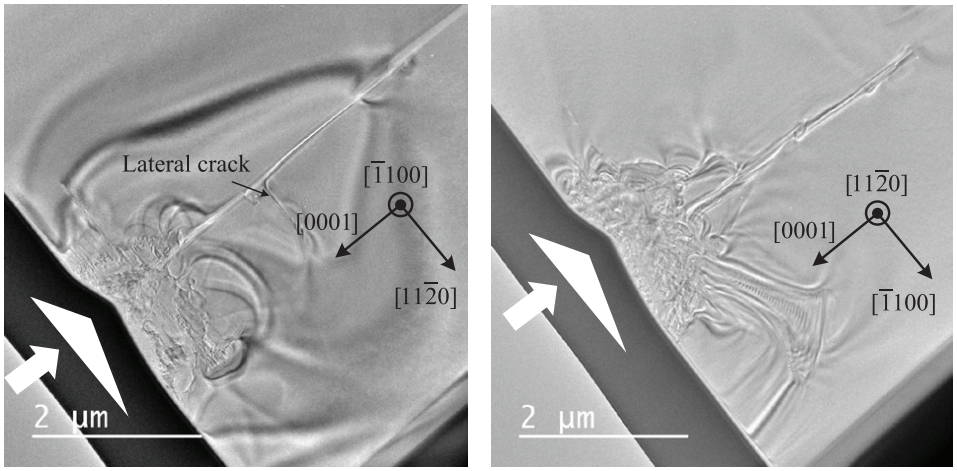

(a) (b)

Figure 8. TEM micrographs of (a) sample D and (b) sample E.

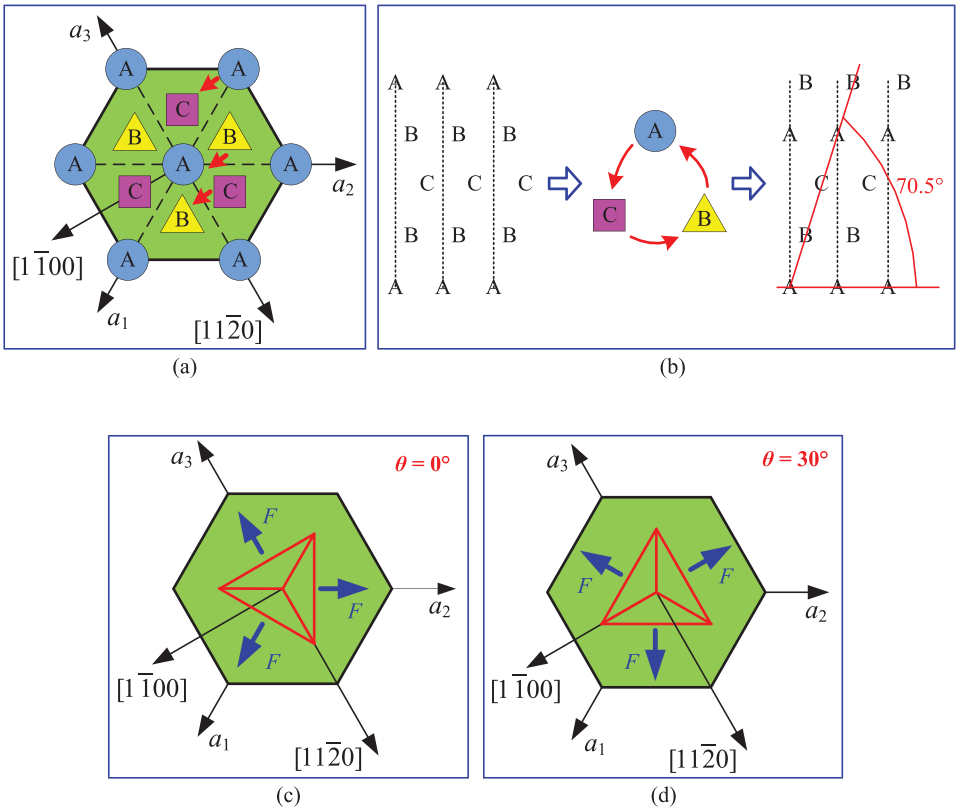

Figure 9. (a) and (b) Schematic diagram illustrating the phase transformation paths from 4H- to 3C–SiC by the slip of $1/3\langle 1\,\bar{1}\,0\,0\rangle$ direction on the $(0\,0\,0\,1)$ plane, i.e. A → C, C → B, B → A. (c) and (d) illustrate the geometrical relationship between the directions of the forces F from the faces of the indenter and the hexagonal crystal structure for $\theta = 0°$ and 30°, respectively.

basic close-packed sites of SiC structures. However, the phase transformation from 4H- to 3C–SiC has never been reported previously for nanoindentation.

The standard stacking sequence for 4H–SiC can be described as A B C B A …, and that for 3C–SiC is A B C …. Previous studies [35] indicated that poly-type transformation in SiC usually resulted from the change of stacking sequences. According to the phase transformation paths proposed in [34], under the complex indentation stress, the atoms in 4H–SiC would change their stacking positions by the slip in $1/3\langle 1\,\bar{1}\,0\,0\rangle$ direction on the $(0\,0\,0\,1)$ plane, i.e. A → C, C → B, B → A, as shown in figures 9(a) and (b). Thus, 3C–SiC structure would be formed by the repeated change of atom sites. Furthermore, the angle between $(1\,1\,1)$ face in the face center cubic structure and $(0\,0\,0\,1)$ face in the hexagonal structure as shown in figure 9(b) is calculated to be 70.5°, agreeing well with the angle between the tilted lattice fringes and $(0\,0\,0\,1)$ face in samples C and E. This further confirms that the phase transformation from 4H- to 3C–SiC occurred during nanoindentation and the tilted lattice fringe in samples C and E was observed in $(1\,1\,1)$ face. The difference in the angle by experimental measurement (~70°) and theoretical calculation (70.5°) possibly results from the measuring error because of the resolution limitation of the TEM used here as well as the residual stress in the deformed region induced by the indenter.

Previous results indicated that the indentation hardness of 4H–SiC strongly depended on the crystal orientation [22, 24, 25]. In this study, the phase transformation of 4H–SiC during nanoindentation shows a similar dependence on the crystal orientation, suggesting that it is closely related to the change of indentation hardness for various crystal orientations. The dependence of phase transformation and indentation hardness on the crystal orientations could be understood by the comparison between figures 9(c) and (d). For $\theta = 0°$, the directions of the forces F from the faces of the indenter coincide with the primary slip directions $\langle 1\,1\,\bar{2}\,0\rangle$ of the hexagonal crystal structure. In this case, the stress can be accommodated easily by dislocation initiation and propagation. Thus, relatively low hardness is obtained and phase transformation is not observed in this case. While for $\theta = 30°$, the directions of the forces F coincide with the $\langle 1\,\bar{1}\,0\,0\rangle$ directions which are the direction for easy occurrence of phase transformation [33, 34]. Thus, the stress generated by the force F readily induces the occurrence of phase transformation from 4H- to 3C–SiC and increased indentation hardness is induced.

4. Conclusions

Microstructural changes of single-crystal 4H–SiC induced by nanoindentation were comparatively investigated under different conditions. The following conclusions were obtained.

(1) Subsurface cracks were initiated at a smaller load than surface cracks.
(2) Subsurface damage region extended far deeper than the indentation depth, involving dislocations occurring along the basal plane, crystal grains rotation and micro-cracks.

(3) By Raman spectra analysis and TEM observation, a phase transformation from 4H–SiC to 3C–SiC was detected when the indenter ridge had an angle of 30° with the $[1\,1\,\bar{2}\,0]$ direction of the specimen, while this phase transformation was not observed for the angle of 0°.
(4) The dependence of phase transformation on the crystal orientation of SiC is closely related to the change of indentation hardness for various crystal orientations.

Acknowledgments

This study has been financially supported by Japan Society for the Promotion of Science, Grant-in-Aid for Exploratory Research 15K13838.

References

[1] Casady J B and Johnson R W 1996 Status of silicon carbide (SiC) as a wide-bandgap semiconductor for high-temperature applications: a review *Solid State Electron.* **39** 1409–22
[2] Yonenaga I, Ohno Y, Taishi T and Tokumoto Y 2009 Recent knowledge of strength and dislocation mobility in wide band-gap semiconductors *Physica* B **404** 4999–5001
[3] Luo X C, Goel S and Reuben R L 2012 A quantitative assessment of nanometric machinability of major polytypes of single crystal silicon carbide *J. Eur. Ceram. Soc.* **32** 3423–34
[4] Goel S, Luo X C, Comley P, Reuben R L and Cox A 2013 Brittle-ductile transition during diamond turning of single crystal silicon carbide *Int. J. Mach. Tools Manuf.* **65** 15–21
[5] Hardin C W, Qu J and Shih A J 2004 Fixed abrasive diamond wire saw slicing of single-crystal silicon carbide wafers *Mater. Manuf. Process.* **19** 355–67
[6] Tan T H and Yan J W 2017 Atomic-scale characterization of subsurface damage and structural changes of single-crystal silicon carbide subjected to electrical discharge machining *Acta Mater.* **123** 362–72
[7] Zhao Y H, Kunieda M and Abe K 2014 Study of EDM cutting of single crystal silicon carbide *Precis Eng.* **38** 92–9
[8] Yan J W and Tan T H 2015 Sintered diamond as a hybrid EDM and grinding tool for the micromachining of single-crystal SiC *CIRP Ann.-Manuf. Technol.* **64** 221–4
[9] Deng H, Hosoya K, Imanishi Y, Endo K and Yamamura K 2015 Electro-chemical mechanical polishing of single-crystal SiC using CeO_2 slurry *Electrochem. Commun.* **52** 5–8
[10] Murata J, Yodogawa K and Ban K 2017 Polishing-pad-free electrochemical mechanical polishing of single-crystalline SiC surfaces using polyurethane–CeO_2 core–shell particles *Int. J. Mach. Tools Manuf.* **114** 1–7
[11] Fischer-Cripps A C 2011 *Nanoindentation* (New York: Springer)
[12] Gerbig Y B, Stranick S J and Cook R F 2011 Direct observation of phase transformation anisotropy in indented silicon studied by confocal Raman spectroscopy *Phys. Rev.* B **83** 205209
[13] Jang J I, Lance M J, Wen S Q, Tsui T Y and Pharr G M 2005 Indentation-induced phase transformations in silicon: influences of load, rate and indenter angle on the transformation behavior *Acta Mater.* **53** 1759–70
[14] Yan J W, Takahashi H, Tamaki J, Gai X H, Harada H and Patten J 2005 Nanoindentation tests on diamond-machined silicon wafers *Appl. Phys. Lett.* **86** 181913
[15] Zeng Z D, Zeng Q S, Mao W L and Qu S X 2014 Phase transitions in metastable phases of silicon *J. Appl. Phys.* **115** 103514
[16] Ruffell S, Bradby J E, Williams J S and Munroe P 2007 Formation and growth of nanoindentation-induced high pressure phases in crystalline and amorphous silicon *J. Appl. Phys.* **102** 063521
[17] Huang H and Yan J W 2015 On the mechanism of secondary pop-out in cyclic nanoindentation of single-crystal silicon *J. Mater. Res.* **30** 1861–8
[18] Huang H and Yan J W 2015 New insights into phase transformations in single crystal silicon by controlled cyclic nanoindentation *Scr. Mater.* **102** 35–8
[19] Szlufarska I, Kalia R K, Nakano A and Vashishta P 2005 Atomistic mechanisms of amorphization during nanoindentation of SiC: a molecular dynamics study *Phys. Rev.* B **71** 174113
[20] Yan J W, Gai X H and Harada H 2010 Subsurface damage of single crystalline silicon carbide in nanoindentation tests *J. Nanosci. Nanotechnol.* **10** 7808–11
[21] Goel S, Yan J W, Luo X C and Agrawal A 2014 Incipient plasticity in 4H–SiC during quasistatic nanoindentation *J. Mech. Behav. Biomed.* **34** 330–7
[22] Matsumoto M, Harada H, Kakimoto K and Yan J W 2016 Study on mechanical properties of single-crystal silicon carbide by nanoindentation *Adv. Mater. Res.* **806** 549–54
[23] Nawaz A, Mao W G, Lu C and Shen Y G 2017 Nano-scale elastic-plastic properties and indentation-induced deformation of single crystal 4H–SiC *J. Mech. Behav. Biomed.* **66** 172–80
[24] Kunka C, Trachet A and Subhash G 2015 Interaction of indentation-induced cracks on single-crystal silicon carbide *J. Am. Ceram. Soc.* **98** 1891–7
[25] Adewoye O O and Page T F 1976 Anisotropic behavior of etched hardness indentations *J. Mater. Sci.* **11** 981–4
[26] Oliver W C and Pharr G M 1992 An improved technique for determining hardness and elastic modulus using load and displacement sensing indentation experiments *J. Mater. Res.* **7** 1564–83
[27] Huang H, Zhao H W, Zhang Z Y, Yang Z J and Ma Z C 2012 Influences of sample preparation on nanoindentation behavior of a Zr-based bulk metallic glass *Materials* **5** 1033–9
[28] Zhang L and Ohmura T 2014 Plasticity initiation and evolution during nanoindentation of an iron–3% silicon crystal *Phys. Rev. Lett.* **112** 145504
[29] Oliver D J, Lawn B R, Cook R F, Reitsma M G, Bradby J E, Williams J S and Munroe P 2008 Giant pop-ins in nanoindented silicon and germanium caused by lateral cracking *J. Mater. Res.* **23** 297–301
[30] Nakashima S and Harima H 1997 Raman investigation of SiC polytypes *Phys. Status Solidi* A **162** 39–64
[31] Nakashima S, Higashihira M, Maeda K and Tanaka H 2003 Raman scattering characterization of polytype in silicon carbide ceramics: comparison with x-ray diffraction *J. Am. Ceram. Soc.* **86** 823–9
[32] Szlufarska I, Kalia R K, Nakano A and Vashishta P 2004 Nanoindentation-induced amorphization in silicon carbide *Appl. Phys. Lett.* **85** 378–80
[33] Okojie R S, Xhang M, Pirouz P, Tumakha S, Jessen G and Brillson L J 2001 Observation of 4H–SiC to 3C–SiC polytypic transformation during oxidation *Appl. Phys. Lett.* **79** 3056–8
[34] Chen B, Wang J, Zhu Y W, Liao X Z, Lu C S, Mai Y W, Ringer S P, Ke F J and Shen Y G 2014 Deformation-induced phase transformation in 4H–SiC nanopillars *Acta Mater.* **80** 392–9
[35] Zhu Y Q, Sekine T, Kobayashi T and Takazawa E 1998 Shock-induced phase transitions among SiC polytypes *J. Mater. Sci.* **33** 5883–90